

# Remarkably Enhanced Dielectric Stability and Energy Storage Properties in BNT-BST Relaxor Ceramics by A-Site Defect Engineering for Pulsed Power Applications

**Zhipeng Li**

Jingdezhen Ceramic University

**Dongxu Li**

Jingdezhen Ceramic University

**Zong-Yang Shen** (✉ [shenzongyang@163.com](mailto:shenzongyang@163.com))

Jingdezhen Ceramic Institute <https://orcid.org/0000-0002-3673-225X>

**Xiaojun Zeng**

Jingdezhen Ceramic University

**Fusheng Song**

Jingdezhen Ceramic University

**Wenqin Luo**

Jingdezhen Ceramic University

**Xingcai Wang**

Chengdu Hongke Electronic Technology Co. Ltd.

**Zhumei Wang**

Jingdezhen Ceramic University

**Yueming Li**

Jingdezhen Ceramic University

---

## Research Article

**Keywords:** relaxor ferroelectrics, energy storage ceramics, ceramic capacitor, BNT, defect engineering

**Posted Date:** June 29th, 2021

**DOI:** <https://doi.org/10.21203/rs.3.rs-659970/v1>

**License:**   This work is licensed under a Creative Commons Attribution 4.0 International License.

[Read Full License](#)

---

**Version of Record:** A version of this preprint was published at Journal of Advanced Ceramics on January 11th, 2022. See the published version at <https://doi.org/10.1007/s40145-021-0532-8>.

# Abstract

Lead-free bulk ceramics for advanced pulsed power capacitors show relatively low recoverable energy storage density ( $W_{\text{rec}}$ ) especially at low electric field condition. To address this challenge, we proposed an A-site defect engineering to optimize the electric polarization behavior by disrupting the orderly arrangement of A-site ions, in which  $\text{Ba}_{0.105}\text{Na}_{0.325}\text{Sr}_{0.245-1.5x}\text{Bi}_{0.5x}\text{TiO}_3$  ( $\text{BNS}_{0.245-1.5x}\text{Bi}_{0.5x}\text{B}_{0.325+x}\text{T}$ ,  $x = 0, 0.02, 0.04, 0.06, 0.08$ ) lead-free ceramics were selected as the representative. The  $\text{BNS}_{0.245-1.5x}\text{Bi}_{0.5x}\text{B}_{0.325+x}\text{T}$  ceramics were prepared by using pressureless solid state sintering and achieved large  $W_{\text{rec}}$  ( $1.8 \text{ J/cm}^3$ ) at a low electric field (@110 kV/cm) when  $x = 0.06$ . The value of  $1.8 \text{ J/cm}^3$  is super high as compared to all other  $W_{\text{rec}}$  in lead-free bulk ceramics under a relatively low electric field ( $< 160 \text{ kV/cm}$ ). Furthermore, a high dielectric constant of  $2930 \pm 15\%$  in a wide temperature range of  $40 \sim 350^\circ\text{C}$  was also obtained in  $\text{BNS}_{0.245-1.5x}\text{Bi}_{0.5x}\text{B}_{0.325+x}\text{T}$  ( $x = 0.06$ ) ceramics. The excellent performances can be attributed to the A-site defect engineering, which can reduce  $P_r$  and improve the thermal evolution of polar nanoregions (PNRs). This work confirms that the  $\text{BNS}_{0.245-1.5x}\text{Bi}_{0.5x}\text{B}_{0.325+x}\text{T}$  ( $x = 0.06$ ) ceramics are desirable for advanced pulsed power capacitors, and will push the development of a series of BNT-based ceramics with high  $W_{\text{rec}}$  and high temperature stability.

## 1 Introduction

Dielectric capacitor is an indispensable component in contemporary electronic devices, which fulfills different functions such as dc blocking, coupling, filtering, and pulse discharge [1, 2]. Considering the complicated working environment, especially high temperature ( $150 \sim 200^\circ\text{C}$ , even to  $300^\circ\text{C}$ ), ceramic dielectrics would be more suitable for energy storage candidates than other polymer materials [3]. Generally, the energy storage properties of ceramic dielectrics can be evaluated by the following equations [4]:

$$W = \int_0^{P_{\text{max}}} E dP \quad (1)$$

$$W_{\text{rec}} = \int_{P_r}^{P_{\text{max}}} E dP \quad (2)$$

$$\eta = \frac{W_{\text{rec}}}{W} \times 100\% \quad (3)$$

where  $W$ ,  $W_{\text{rec}}$ ,  $h$ ,  $E$ ,  $dP$ ,  $P_{\text{max}}$ , and  $P_r$  denote total energy storage density, recoverable energy storage density, energy efficiency, applied external electric field, polarization increment at  $E$ , maximum polarization, and remnant polarization, respectively. Therefore, high  $P_{\text{max}}$ , low  $P_r$ , and high breakdown strengthen  $E_b$  are important factors to achieve high  $W_{\text{rec}}$  [5, 6]. However, high applied electric field may

limit its application in integrated electronic circuits, as well as in wearable or implantable devices requiring low electric field. Pb-based relaxor ferroelectric and antiferroelectric ceramics had been considered as potential candidates, while the toxic of Pb limits its application [7, 8]. It is urgent to design and develop new Pb-free systems with high  $W_{\text{rec}}$  especially under relatively low electric field.

Bismuth sodium titanate ( $\text{Bi}_{0.5}\text{Na}_{0.5}\text{TiO}_3$ , BNT) possesses characteristics of high  $P_{\text{max}}$  and complicated phase structure, and hence is considered as a promising potential energy storage ferroelectric material [9-11]. Noted that a high  $P_r$  and poor sintering behavior of pure BNT ceramic result in a low  $W_{\text{rec}}$ . Different methods, therefore, are utilized to improve  $W_{\text{rec}}$  such as chemical doping, glass modification, multilayer structure design, advanced sintering technology [12-17]. For chemical doping, it can be divided into chemical equivalent and aliovalent doping. Especially, the chemical aliovalent doping includes “donor” and “acceptor” doping, which can induce different types of defects and improve the properties of materials. For example, Cao et al. used  $\text{Mn}^{2+}$  as acceptor dopant to substitute B-site ions of 0.7[0.94NBT-0.06BT]-0.3ST ceramic, acquired a high  $W_{\text{rec}}$  of 1.06 J/cm<sup>3</sup> [18]. Xu et al. found a pinched  $P$ - $E$  loop behavior in Ta donor doped BNT-0.06BT ferroelectric ceramic [19]. It can be observed that defect engineering can effectively improve energy storage properties by forming defect dipoles. However, it should be pointed out that a few reports on the chemical defects by adjusting element ratio in composition to optimize the energy storage properties of BNT-based ceramics.

Based on our previous work, a binary solid solution of  $(\text{Bi}_{0.5}\text{Na}_{0.5})_{0.65}(\text{Ba}_{0.3}\text{Sr}_{0.7})_{0.35}\text{TiO}_3$  (BNT-BST) is considered as a good energy storage material due to “clamped” behavior in  $P$ - $E$  loop and high dielectric constant  $\epsilon_r$  (~4000) at room temperature [20, 21]. However, its relatively high  $P_r$  and poor dielectric temperature stability make it hard to obtain high  $W_{\text{rec}}$ . Based on the above considerations, we proposed A-site defect engineering, i.e., to adjust Bi/Sr ratio by generating different concentrations of  $\text{Sr}^{2+}$  vacancy to enhance  $W_{\text{rec}}$  in this work. Consequently, phase structure, micrograph, dielectric temperature stability and energy storage properties of  $\text{Ba}_{0.105}\text{Na}_{0.325}\text{Sr}_{0.245-1.5x}\delta_{0.5x}\text{Bi}_{0.325+x}\text{TiO}_3$  ceramics are investigated.

## 2 Experimental Procedures

$\text{Ba}_{0.105}\text{Na}_{0.325}\text{Sr}_{0.245-1.5x}\delta_{0.5x}\text{Bi}_{0.325+x}\text{TiO}_3$  ( $\text{BNS}_{0.245-1.5x}\delta_{0.5x}\text{B}_{0.325+x}\text{T}$ ,  $x = 0, 0.02, 0.04, 0.06, 0.08$ ) ceramics were fabricated using a solid-state process. Raw materials  $\text{Bi}_2\text{O}_3$  (99.9%),  $\text{Na}_2\text{CO}_3$  (99.8%),  $\text{TiO}_2$  (99.9%),  $\text{BaCO}_3$  (99.0%), and  $\text{SrCO}_3$  (99.9%) (Purchased from Sinopharm Chemical Reagent Co. Ltd., Shanghai, China) were weighted according to stoichiometric formula and mixed in planetary ball mill for 24 h with zirconia balls in ethanol. After separating the balls, the mixtures were dried, calcined at 800 °C for 3 h, and then milled again for 24 h. The powder was compacted into pellets of 13 mm in diameter and about 1 mm thickness under  $120 \pm 10$  MPa pressure after granulated by adding polyvinyl alcohol solution (PVA, 5 wt%). The disks were preheated at 650 °C for 2 h to remove PVA binder, and finally sintered at 1180 ~ 1240 °C for 2 h in air followed by furnace cooling.

The phase structure evolution was identified using X-ray diffraction (XRD, D8-Advance, Bruker, Germany) with Cu K $\alpha$  radiation and Raman spectroscopy (LabRAM HR800, HORIBA). The microstructure features of the ceramic sample were observed by a scanning electron microscope (SEM, JSM-6700F, JEOL, Japan) after polishing and thermally-etching. For electrical performance testing, ceramic samples were polished to smooth and parallel in both surfaces and then painted Ag electrode on both sides. The dielectric properties of ceramics were measured using a precision impedance analyzer (HP4294A, Agilent) over a temperature range from - 100 °C to 400 °C. For *P-E* loop and charge-discharge measurements, the ceramic samples were polished and covered a central electrode with margin blank on both sides. The *P-E* hysteresis loops and *I-E* curves were examined using a ferroelectric analyzer at 10 Hz (Trek model 609B) based on a standard Sawyer-Tower circuit. The temperature dependent charge-discharge capability was tested using a designed RLC circuit (CFD-003, Tongguo Technology, Shanghai, China) being connected to a temperature controlled chamber.

### 3 Results And Discussion

Figure 1(a) shows XRD patterns of BNS $_{0.245-1.5x}$ ǒ $_{0.5x}$ B $_{0.325+x}$ T ceramics at  $2\theta = 20^\circ-80^\circ$ . All samples are pure pseudocubic perovskite structure without trace of any other secondary phases. As seen from Fig. 1(b), the diffraction peak (200) slightly shifts toward a high angle with the increase of *x* value, indicating cell volume gradually decreases. This phenomenon should be attributed to the following reasons: the one is that the replacement of Bi $^{3+}$  ions with a smaller ionic radius ( $r_i=1.35 \text{ \AA}$ , CN = 12) to Sr $^{2+}$  ( $r_i=1.44 \text{ \AA}$ , CN = 12) with a larger one, and the other is that Sr vacancy content gradually increases with *x* value, while the existence of vacancy provides a space for lattice contraction.

It is well known that Raman spectroscopy is an effective tool to investigate the crystalline structure information and phase transition. Figure 2(a) shows Raman spectra of BNS $_{0.245-1.5x}$ ǒ $_{0.5x}$ B $_{0.325+x}$ T ceramics at room temperature. Generally, BNT material possesses 16 active phonon modes, and the irreducible representation is  $\Gamma_{\text{Raman}} = 4A_1 + 1B_1 + 3B_2 + 8E$  based on the group theory [22, 23]. Figure 2(b) displays the fitted Raman pattern only includes 8 modes for pure BNT-BST ceramics at room temperature, which should be attributed to disorder occupation of ions at A-site and polycrystalline feature of ceramics. In order to better illustrate the results, four main regions can be classified into the Raman spectra: (A) The modes below  $200 \text{ cm}^{-1}$  ( $\nu_1, \nu_2$ ) are related to A-site cations vibration, including Bi $^{3+}$ , Na $^+$ , Ba $^{2+}$ , and Sr $^{2+}$  ions; (B) The modes around  $200 \sim 400 \text{ cm}^{-1}$  ( $\nu_3, \nu_4$ ) should be associated with the vibration of Ti-O bond; (C) The modes from  $400$  to  $700 \text{ cm}^{-1}$  ( $\nu_5, \nu_6$ ) are related to [TiO $_6$ ] vibrations, namely the breathing and stretching of the oxygen octahedral; (D) The modes above  $700 \text{ cm}^{-1}$  ( $\nu_7, \nu_8$ ) are ascribed to the super-position of vibration A $_1$  (longitudinal optical) and E (longitudinal optical) overlapping bands [23–26]. The Raman patterns are decomposed by Lorentz peak fitting to investigate the effect of *x* value on the vibration modes. The fitted Raman patterns for the represented BNS $_{0.245-1.5x}$ ǒ $_{0.5x}$ B $_{0.325+x}$ T ceramics with  $x = 0$  and  $x = 0.06$  are shown in Figs. 2(b)-2(c), respectively. With the increase of the *x* value, the  $\nu_2$  phonon mode's wave number presents an obvious shifting upward

tendency and signal intensity enhance as shown in Fig. 2(d), which should be owing to the increase of Sr vacancy. Meanwhile, the  $\nu_3$  phonon mode's wave number shows a shifting upward as well, which due to the tilt or twist of the Ti-O bond. This may be ascribed to the increase of Sr vacancies and empty in lattices. Furthermore, the wave number and signal intensity of the  $\nu_6$  phonon mode remain basically unchanged, while the wave number of the  $\nu_5$  phonon mode decreases slowly, as shown in Fig. 2(d). These changes could be due to structural transition, possibly due to  $\text{TiO}_6$  octahedral distortion caused by the increase of Sr vacancy and empty in lattices with  $x$ .

Figure 3 displays the micrograph feature of polished and thermally-etched  $\text{BNS}_{0.245-1.5x}\text{Bi}_{0.5x}\text{B}_{0.325+x}\text{T}$  ceramics. It can be seen from Figs. 3(a)-3(e) that  $\text{BNS}_{0.245-1.5x}\text{Bi}_{0.5x}\text{B}_{0.325+x}\text{T}$  ceramics possesses uniform grains and extremely high density. As  $x$  value increases, the grain size gradually increases (see Fig. 3f), which should be attributed to the following two reasons: the one is that  $\text{Bi}^{3+}$  replaces the A-site ion, the lattice shrinkage will cause stress, and the other is that  $\text{Bi}^{3+}$  replaces  $\text{Sr}^{2+}$ , in order to maintain charge balance, defects such as Sr vacancy and empty lattices will be formed, and stress will also be generated, which accelerates the mass transfer rate between particles and weakens the competition with the adjacent grains, leading to accelerated grain growth and densification promotion of ceramics during the sintering process [27].

Figures 4(a)-4(e) show temperature dependent of dielectric properties for  $\text{BNS}_{0.245-1.5x}\text{Bi}_{0.5x}\text{B}_{0.325+x}\text{T}$  ceramics with different  $x$  values at frequencies of 1 kHz, 10 kHz, 100 kHz, and 1 MHz. It should be mentioned that relaxor ferroelectric has two obvious characteristics: one is  $T_m$  shifts toward high temperature with increasing frequency, and the other is dielectric constant at  $T_m$  decreases with the increase of frequency whereas that of loss tangent follows the reverse order. Meanwhile, a modified Curie-Weiss law is applied to evaluate the relaxor characteristic [28]:

$$\frac{1}{\epsilon_r} - \frac{1}{\epsilon_m} = \frac{(T - T_m)^\gamma}{C} \quad (4)$$

where  $\epsilon_r$ ,  $T_m$ ,  $C$  are the relative dielectric constant, the absolute temperature corresponding to the maximum dielectric constant  $\epsilon_m$ , the Curie constant, respectively. The diffuseness factor  $\gamma$  decreases with decreasing relaxor degree, varies between 1 (for normal ferroelectric) and 2 (for ideal relaxor ferroelectric) [29]. With increasing  $x$  value,  $\gamma$  value increases from 1.71 to 2.00, indicating relaxor characteristic is effectively enhanced, for pure BNT-BST ceramics, one dielectric peak at  $T_m$  and obvious relaxor behavior below  $T_m$  can be observed. After composition modification, wave-like double peaks can be found in dielectric spectra, and corresponding temperature is named as  $T_{m1}$  and  $T_{m2}$ , respectively. Noted that dielectric relaxor behavior only exists at a temperature below  $T_{m1}$ , and thus dielectric peak at  $T_{m1}$  is similar to that at  $T_m$ . Thus, a new dielectric peak at  $T_{m2}$  should be induced by Bi-Sr ratio change.

Temperature stability of dielectric constant (TCC) is a crucial factor to influence its application scenes. In general, it can be calculated by the equation as follows:

$$TCC = \frac{(\varepsilon - \varepsilon_{base})}{\varepsilon_{base}} \quad (4)$$

where  $\varepsilon_{base}$  denote dielectric constant at a based temperature, other is accorded to above mentioned. As  $x$  value increases, the dielectric peak at  $T_{m1}$  is suppressed, while the temperature difference  $\Delta T (T_{m2} - T_{m1})$  is gradually enhanced, which is beneficial for enhancing temperature stability. Fig. 4(f) shows TCC of  $BNS_{0.245-1.5x}\delta_{0.5x}B_{0.325+x}T$  ceramics with different  $x$  values chosen 150 °C as based temperature. With increasing  $x$  value, dielectric temperature stability is effectively enhanced especially at high temperature, which is attributed to the appearance of a new dielectric peak at  $T_{m2}$ . For  $x = 0.06$  composition, a wide temperature range of TCC at  $\pm 15\%$  corresponds to 40~350 °C.

In order to further explore the reason for generating dielectric peak at  $T_{m2}$ , a variable Raman spectrum is used. Fig. 5 shows Raman spectra and wave number of Raman peaks of  $BNS_{0.245-1.5x}\delta_{0.5x}B_{0.325+x}T$  ceramics with  $x = 0.06$  over a temperature range from room temperature to 275 °C. As temperature increases, the signals of modes  $\nu_2$  and  $\nu_6$  gradually present a disappeared tendency, while other modes change slightly, as shown in Fig. 5(a). All modes display a decreased tendency, while no abruptly change in wave number (Fig. 5b). The result illustrates that mode  $\nu_2$  and  $\nu_6$  is sensitive to phase structure of  $BNS_{0.245-1.5x}\delta_{0.5x}B_{0.325+x}T$  ceramics with  $x = 0.06$ . The slow transition of modes  $\nu_2$  and  $\nu_6$  both demonstrate phase structure of  $x = 0.06$  composition just have a slight change. Therefore, it can be concluded that the new dielectric peak at  $T_{m2}$  should be attributed to the thermal evolution of PNRs affected by the concentration of Sr vacancies.

Figure 6(a) shows  $P$ - $E$  loops of  $BNS_{0.245-1.5x}\delta_{0.5x}B_{0.325+x}T$  ceramics at 60 kV/cm and room temperature. As  $x$  value increases,  $P$ - $E$  loops gradually go slim, which is beneficial for improving energy storage properties, the maximum polarization at a given electric field slightly decreases with the increase of  $x$  value. Combined with  $I$ - $E$  loops at the same conditions, current peaks gradually diffuse, and corresponding intensity decreases, indicating the relaxor characteristic is enhanced [30]. In addition,  $P_{max}$ ,  $P_r$  and  $P_{max} - P_r$  versus  $x$  value for  $BNS_{0.245-1.5x}\delta_{0.5x}B_{0.325+x}T$  ceramics at 60 kV/cm is exhibited in Fig. 6(b). A relatively high  $P_{max} - P_r$  of 27.52  $\mu\text{C}/\text{cm}^2$  can be obtained at  $x = 0.06$  composition due to a rapid decrease in  $P_r$ , because the PNRs are dynamic sensitive to external electric field stimuli. Figs. 6(c)-6(d) show energy efficiency  $h$  and recoverable energy density  $W_{rec}$  of  $BNS_{0.245-1.5x}\delta_{0.5x}B_{0.325+x}T$  ceramics at different electric fields, respectively. As  $x$  value increases,  $h$  presents an increased tendency obtaining a high value for  $x = 0.06$  composition, and then decreases again with further increasing  $x$  value. Meanwhile,  $BNS_{0.245-1.5x}\delta_{0.5x}B_{0.325+x}T$  ceramics with  $x = 0.06$  possess a maximum  $W_{rec}$  of 1.8  $\text{J}/\text{cm}^3$  only at a low electric field of 110 kV/cm, as shown in Fig. 6(d).

In order to investigate the working stability at different external fields, temperature, frequency and electric fatigue dependent energy storage properties of  $BNS_{0.245-1.5x}\delta_{0.5x}B_{0.325+x}T$  ceramics with  $x = 0.06$  have been examined. Fig. 7(a) shows  $P$ - $E$  loops of  $x = 0.06$  ceramics over a temperature range of 30~150 °C at

60 kV/cm and 10 Hz. As temperature increases,  $P$ - $E$  loops gradually go slim, and keep a high  $P_s$  and low  $P_r$ . Therefore,  $W_{rec}$  and  $h$  of  $x = 0.06$  ceramics possess good temperature stability, as exhibited in Fig. 7(b). Meanwhile, frequency dependent  $P$ - $E$  loops of  $x = 0.06$  ceramics at 60 kV/cm are displayed in Fig. 7(c). It can be seen that energy loss has a slight increase tendency during discharge process, which may be related to vacancy defect pin domain wall.  $W_{rec}$  and  $h$  of  $x = 0.06$  ceramics, therefore, show a slight decrease in value at frequency of 1~100 Hz, as shown in Fig. 7(d). Finally,  $P$ - $E$  loops as functions of cycle numbers and corresponding  $W_{rec}$  and  $h$  for  $x = 0.06$  ceramics are illustrated in Figs. 7(e)-(f), respectively. Noted that polarization of  $x = 0.06$  ceramics keeps a stable value at 10 Hz after  $10^5$  electric cycles. Obviously,  $x = 0.06$  ceramics possess a good fatigue endurance, and  $W_{rec}$  and  $h$  as functions of cycles are illustrated in Fig. 7(f).

Charge-discharge characteristic is an essential factor for dielectric materials to evaluate its energy storage capabilities, and thus charge-discharge measurement is fulfilled at a specified circuit. Generally, discharge energy density  $W_d$  can be calculated by the equation as following [31]:

$$W_d = \frac{R \int i^2 dt}{V}$$

where  $R$  is load resistance (100  $\Omega$ ),  $i$  is the maximum discharge current, and  $V$  is the effective volume of ceramic between two electrodes. Figs. 8(a)-(b) show room temperature underdamped discharge waveform and corresponding  $W_d$  of  $\text{BNS}_{0.245-1.5x}\text{B}_{0.5x}\text{B}_{0.325+x}\text{T}$  ceramics with  $x = 0.06$  ceramics at different electric fields, respectively. As the electric field increases, the maximum discharge current  $I_{max}$  and  $W_d$  both gradually enhances. It should be mentioned that  $W_d$  is less than  $W_{rec}$  at the same electric field for  $x = 0.06$  compositions. This may be attributed to the following two reasons [32]: the one is that the domain can not switch quickly to respond to the external electric field, and the other is that equivalent series resistance (ESR) generate joule heat during charge-discharge process. The discharge rate is characterized by evaluating factor  $t_{0.9}$  (dashed line in Fig. 8b), which represents the time needed for releasing 90% of all stored energy [33]. Fig. 8(b) shows that  $t_{0.9}$  is about 0.1  $\mu\text{s}$  for  $x = 0.06$  ceramics at room temperature, which illustrates energy can be released by a pulse current way in a short time. Variable temperature discharge current curves as function time for  $\text{BNS}_{0.245-1.5x}\text{B}_{0.5x}\text{B}_{0.325+x}\text{T}$  ceramics with  $x = 0.06$  ceramics are displayed in Fig. 8(c). As temperature increases, the maximum discharge current  $I_{max}$  basically keeps a stable value while  $W_d$  possesses an obvious enhancement as shown in Fig. 8(d). The discharge capability of  $x = 0.06$  ceramics possesses good temperature stability, which is beneficial for the application in high temperature environment.

To better evaluate the energy storage properties of  $\text{BNS}_{0.245-1.5x}\text{B}_{0.5x}\text{B}_{0.325+x}\text{T}$  ceramics, we compare  $W_{rec}$  and  $E_{max}$  of  $x = 0.06$  and 0.08 composition with some lead-free ceramic bulks reported previously [34-44]. It can be seen from Fig. 9(a) that a large  $W_{rec}$  ( $>1.5 \text{ J/cm}^3$ ) usually requires a high  $E_b$  ( $>160 \text{ kV/cm}$ ) to produce high polarization, especially for some BT-based and KNN-based materials. In this work, a high

$W_{\text{rec}}$  can be achieved under a relatively low electric field, which exceeds other BNT-based energy storage ceramics at the same electric field, even other lead-free systems. With further comparing  $W_{\text{rec}}$  and  $h$  of different compositions, as shown in Fig. 9(b). It should be pointed that high  $W_{\text{rec}}$  and  $h$  is hard to obtain simultaneously in one system influenced by heat loss at electric field. Note that  $\text{BNS}_{0.1555}\delta_{0.03}\text{B}_{0.385}\text{T}$  ( $x = 0.06$ ) ceramics possess a relatively high  $W_{\text{rec}}$  ( $>1.5 \text{ J/cm}^3$ ), together with high  $h$  ( $>70\%$ ) under relatively low electric field ( $<160 \text{ kV/cm}$ ), demonstrating it is potential to obtain both high  $W_{\text{rec}}$  and  $h$ , which should be a promising candidate for power ceramic capacitors application.

## 4 Conclusions

In this work, A-site defect engineering was proposed to improve the energy storage performance of  $\text{BNS}_{0.245-1.5x}\delta_{0.5x}\text{B}_{0.325+x}\text{T}$  lead-free ceramics. High recoverable energy density of  $1.8 \text{ J/cm}^3$  under low electric field ( $@110 \text{ kV/cm}$ ) and energy efficiency of 72% are achieved simultaneously in the sample with  $x = 0.06$ . This good energy storage performance is attributed to the A-site defect engineering that can reduce  $P_r$ . The ceramic also exhibits satisfactory thermal, frequency, and cycling stabilities as well as a high charge-discharge rate.  $\text{BNS}_{0.245-1.5x}\delta_{0.5x}\text{B}_{0.325+x}\text{T}$  ( $x = 0.06$ ) ceramics show a high dielectric constant of  $2930 \pm 15\%$  in a wide temperature range of  $40 \sim 350^\circ\text{C}$ . This high-temperature stability is attributed to the A-site defect engineering, which can improve the thermal evolution of PNRs. All these advantages indicate that  $\text{BNS}_{0.245-1.5x}\delta_{0.5x}\text{B}_{0.325+x}\text{T}$  ceramics is suitable for solid state pulse power ceramic capacitors, and A-site defect engineering is a robust strategy to improve the  $W_{\text{rec}}$  and high-temperature stability of lead-free ceramics.

## Declarations

## Acknowledgments

This work was financially supported by National Natural Science Foundation of China (51767010).

## References

1. Sarjeant WJ, Clelland IW (2001) Price RA Capacitive components for power electronics. P IEEE 89:846–855
2. Khanchaitit P, Han K, Gadinski MR et al (2013) Ferroelectric polymer networks with high energy density and improved discharged efficiency for dielectric energy storage. Nat Commun 4:2845
3. Yao ZH, Song Z, Hao H et al (2017) Homogeneous/Inhomogeneous-Structured Dielectrics and their Energy-Storage Performances. Adv Mater 29:1601727
4. Palneedi H, Peddigari M, Hwang G-T et al (2018) High-Performance Dielectric Ceramic Films for Energy Storage Capacitors: Progress and Outlook. Adv Funct Mater 28:1803665

5. Pan H, Li F, Liu Y et al (2019) Ultrahigh–energy density lead-free dielectric films via polymorphic nanodomain design. *Science* 365:578–582
6. Yan J, Wang Y, Wang C-M, Ouyang (2021) Boosting energy storage performance of low-temperature sputtered  $\text{CaBi}_2\text{Nb}_2\text{O}_9$  thin film capacitors via rapid thermal annealing. *J Adv Ceram* 10:627–635
7. Peng B, Tang S, Lu L et al (2020) Low-temperature-poling awakened high dielectric breakdown strength and outstanding improvement of discharge energy density of  $(\text{Pb},\text{La})(\text{Zr},\text{Sn},\text{Ti})\text{O}_3$  relaxor thin film. *Nano Energy* 77:105132
8. Dong G, Fan H, Liu L et al (2021) Large electrostrain in  $\text{Bi}_{1/2}\text{Na}_{1/2}\text{TiO}_3$ -based relaxor ferroelectrics: A case study of  $\text{Bi}_{1/2}\text{Na}_{1/2}\text{TiO}_3$ - $\text{Bi}_{1/2}\text{K}_{1/2}\text{TiO}_3$ - $\text{Bi}(\text{Ni}_{2/3}\text{Nb}_{1/3})\text{O}_3$  ceramics. *J Materiomics* 7:593–602
9. Rödel J, Jo W, Seifert KTP et al (2009) Perspective on the Development of Lead-free Piezoceramics. *J Am Ceram Soc* 92:1153–1177
10. Suchanicz J, Kluczevska-Chmielarz K, Sitko D (2021) Jagło G Electrical transport in lead-free  $\text{Na}_{0.5}\text{Bi}_{0.5}\text{TiO}_3$  ceramics. *J Adv Ceram* 10:152–165
11. Li DX, Shen Z-Y, Li ZP et al (2020) P-E hysteresis loop going slim in  $\text{Ba}_{0.3}\text{Sr}_{0.7}\text{TiO}_3$ -modified  $\text{Bi}_{0.5}\text{Na}_{0.5}\text{TiO}_3$  ceramics for energy storage applications. *J Adv Ceram* 9:183–192
12. Sung YS, Kim JM, Cho JH et al (2011) Effects of Bi nonstoichiometry in  $(\text{Bi}_{0.5+x}\text{Na})\text{TiO}_3$  ceramics. *Appl Phys Lett* 98:012902
13. Gao F, Dong X, Mao C et al (2011) Energy-Storage Properties of  $0.89\text{Bi}_{0.5}\text{Na}_{0.5}\text{TiO}_3$ - $0.06\text{BaTiO}_3$ - $0.05\text{K}_{0.5}\text{Na}_{0.5}\text{NbO}_3$  Lead-Free Anti-ferroelectric Ceramics. *J Am Ceram Soc* 94:4382–4386
14. Chen X, Li X, Zhou H et al (2019) Phase evolution, microstructure, electric properties of  $(\text{Ba}_{1-x}\text{Bi}_{0.67x}\text{Na}_{0.33x})(\text{Ti}_{1-x}\text{Bi}_{0.33x}\text{Sn}_{0.67x})\text{O}_3$  ceramics. *J Adv Ceram* 8:427–437
15. Lu X, Xu J, Yang L et al (2016) Energy storage properties of  $(\text{Bi}_{0.5}\text{Na}_{0.5})_{0.93}\text{Ba}_{0.07}\text{TiO}_3$  lead-free ceramics modified by La and Zr co-doping. *J Materiomics* 2:87–93
16. Li J, Li F, Xu Z, Zhang SM (2018) Lead-Free Ceramic Capacitors with Ultrahigh Energy Density and Efficiency. *Adv Mater* 30:1802155
17. Shen Z-Y, Wang Y, Tang Y et al (2019) Glass modified barium strontium titanate ceramics for energy storage capacitor at elevated temperatures. *J Materiomics* 5:641–648
18. Cao W, Li W, Feng Y et al (2016) Defect dipole induced large recoverable strain and high energy-storage density in lead-free  $\text{Na}_{0.5}\text{Bi}_{0.5}\text{TiO}_3$ -based systems. *Appl Phys Lett* 108:202902
19. Xu Y, Liu X, Wang G et al (2016) Antiferroelectricity in tantalum doped  $(\text{Bi}_{0.5}\text{Na}_{0.5})_{0.94}\text{Ba}_{0.06}\text{TiO}_3$  lead-free ceramics. *Ceram Int* 42:4313–4322
20. Li DX, Shen Z-Y, Li ZP et al (2019) Structural evolution, dielectric and ferroelectric properties of  $(1-x)\text{Bi}_{0.5}\text{Na}_{0.5}\text{TiO}_3$ - $x\text{Ba}_{0.3}\text{Sr}_{0.7}\text{TiO}_3$  ceramics. *J Mater Sci: Mater Electron* 30:5917–5922
21. Li DX, Shen Z-Y, Li ZP et al (2020) Effect of  $(\text{Nb}_{2/3}\text{Mg}_{1/3})^{4+}$  complex on the dielectric and ferroelectric properties of  $(\text{Ba}_{0.3}\text{Sr}_{0.7})_{0.35}(\text{Bi}_{0.5}\text{Na}_{0.5})_{0.65}\text{TiO}_3$  ceramics for energy storage. *J Mater Sci: Mater*

22. Li Q, Wang C, Zhang W, Fan H (2019) Influence of compositional ratio K/Na on structure and piezoelectric properties in  $[(\text{Na}_{1-x}\text{K}_x)_{0.5}\text{Bi}_{0.5}]\text{Ti}_{0.985}\text{Ta}_{0.015}\text{O}_3$  ceramics. *J Mater Sci* 54:4523–4531
23. Rout D, Moon K-S, Kang S-JL, Kim IW (2010) Dielectric and Raman scattering studies of phase transitions in the  $(100-x)\text{Na}_{0.5}\text{Bi}_{0.5}\text{TiO}_3-x\text{SrTiO}_3$  system. *J Appl Phys* 108:084102
24. McLaughlin K, Pascual-Gonzalez C, Wang D (2019) Feteira A Site occupancy and electric-field induced strain response of Er-doped  $(\text{Bi}_{0.4}\text{Na}_{0.4}\text{Sr}_{0.2})\text{TiO}_3$  ceramics. *J Alloy Compd* 779:7–14
25. Tripathy SN, Mishra KK, Sen S (2014) Pradhan DK Dielectric and Raman Spectroscopic Studies of  $\text{Na}_{0.5}\text{Bi}_{0.5}\text{TiO}_3-\text{BaSnO}_3$  Ferroelectric System. *J Am Ceram Soc* 97:1846–1854
26. Petzelt J, Kamba S, Fábry J et al Infrared, Raman and high-frequency dielectric spectroscopy and the phase transitions in  $\text{Na}_{1/2}\text{Bi}_{1/2}\text{TiO}_3$ . *J Phys: Condens Mat* 2004, 16: 2719–2731
27. Xu Q, Ding S, Song T et al (2013) Effect of  $\text{Nd}_2\text{O}_3$  Doping on Microstructure and Dielectric Properties of BCZT Ceramics. *J Chin Ceram Soc* 41:292–297
28. Li DX, Shen Z-Y, Li ZP et al (2020) Optimization of polarization behavior in  $(1-x)\text{BSBNT}-x\text{NN}$  ceramics for pulsed power capacitors. *J Mater Chem C* 8:7650–7657
29. Huang Y, Li F, Hao H et al (2019)  $(\text{Bi}_{0.51}\text{Na}_{0.47})\text{TiO}_3$  based lead free ceramics with high energy density and efficiency. *J Materiomics* 5:385–393
30. Xu Q, Li T, Hao H et al (2015) Enhanced energy storage properties of  $\text{NaNbO}_3$  modified  $\text{Bi}_{0.5}\text{Na}_{0.5}\text{TiO}_3$  based ceramics. *J Eur Ceram Soc* 35:545–553
31. Tian J, Wang S, Jiang T et al (2019) Dielectric characterization of a novel  $\text{Bi}_2\text{O}_3-\text{Nb}_2\text{O}_5-\text{SiO}_2-\text{Al}_2\text{O}_3$  glass-ceramic with excellent charge-discharge properties. *J Eur Ceram Soc* 39:1164–1169
32. Yang L, Kong X, Li F et al (2019) Perovskite lead-free dielectrics for energy storage applications. *Prog Mater Sci* 102:72–108
33. Ahn CW, Amarsanaa G, Won SS et al (2015) Antiferroelectric Thin-Film Capacitors with High Energy-Storage Densities, Low Energy Losses, and Fast Discharge Times. *ACS Appl Mater Inter* 7:26381–26386
34. Hu Q, Jin L, Wang T et al (2015) Dielectric and temperature stable energy storage properties of  $0.88\text{BaTiO}_3-0.12\text{Bi}(\text{Mg}_{1/2}\text{Ti}_{1/2})\text{O}_3$  bulk ceramics. *J Alloy Compd* 640:416–420
35. Benyoussef M, Zannen M, Belhadi J et al (2018) Dielectric, ferroelectric, and energy storage properties in dysprosium doped sodium bismuth titanate ceramics. *Ceram Int* 44:19451–19460
36. Wei M, Zhang J, Wu K, et al. Effect of  $\text{BiMO}_3$  (M = Al, In, Y, Sm, Nd, and La) doping on the dielectric properties of  $\text{BaTiO}_3$  ceramics. *Ceram Int* 2017, **43**: 9593–9599
37. Wang B, Luo L, Jiang X et al (2014) Energy-storage properties of  $(1-x)\text{Bi}_{0.47}\text{Na}_{0.47}\text{Ba}_{0.06}\text{TiO}_3-x\text{KNbO}_3$  lead-free ceramics. *J Alloy Compd* 585:14–18
38. Zhang M, Yang H, Li D (2020) Lin Y Excellent energy density and power density achieved in  $\text{K}_{0.5}\text{Na}_{0.5}\text{NbO}_3$ -based ceramics with high optical transparency. *J Alloy Compd* 829:154565

39. Yang Z, Gao F, Du H et al (2019) Grain size engineered lead-free ceramics with both large energy storage density and ultrahigh mechanical properties. *Nano Energy* 58:768–777
40. Zhao X, Zhou Z, Liang R et al (2017) High-energy storage performance in lead-free  $(1-x)\text{BaTiO}_3\text{-}x\text{Bi}(\text{Zn}_{0.5}\text{Ti}_{0.5})\text{O}_3$  relaxor ceramics for temperature stability applications. *Ceram Int* 43:9060–9066
41. Wu L, Wang X (2016) Li L Lead-free  $\text{BaTiO}_3\text{-Bi}(\text{Zn}_{2/3}\text{Nb}_{1/3})\text{O}_3$  weakly coupled relaxor ferroelectric materials for energy storage. *RSC Adv* 6:14273–14282
42. Shao T, Du H, Ma H et al (2017) Potassium–sodium niobate based lead-free ceramics: novel electrical energy storage materials. *J Mater Chem A* 5:554–563
43. Wang T, Jin L, Li C et al (2015) Relaxor Ferroelectric  $\text{BaTiO}_3\text{-Bi}(\text{Mg}_{2/3}\text{Nb}_{1/3})\text{O}_3$  Ceramics for Energy Storage Application. *J Am Ceram Soc* 98:559–566
44. Qi H (2019) Zuo R Linear-like lead-free relaxor antiferroelectric  $(\text{Bi}_{0.5}\text{Na}_{0.5})\text{TiO}_3\text{-NaNbO}_3$  with giant energy-storage density/efficiency and super stability against temperature and frequency. *J Mater Chem A* 7:3971–3978

## Figures

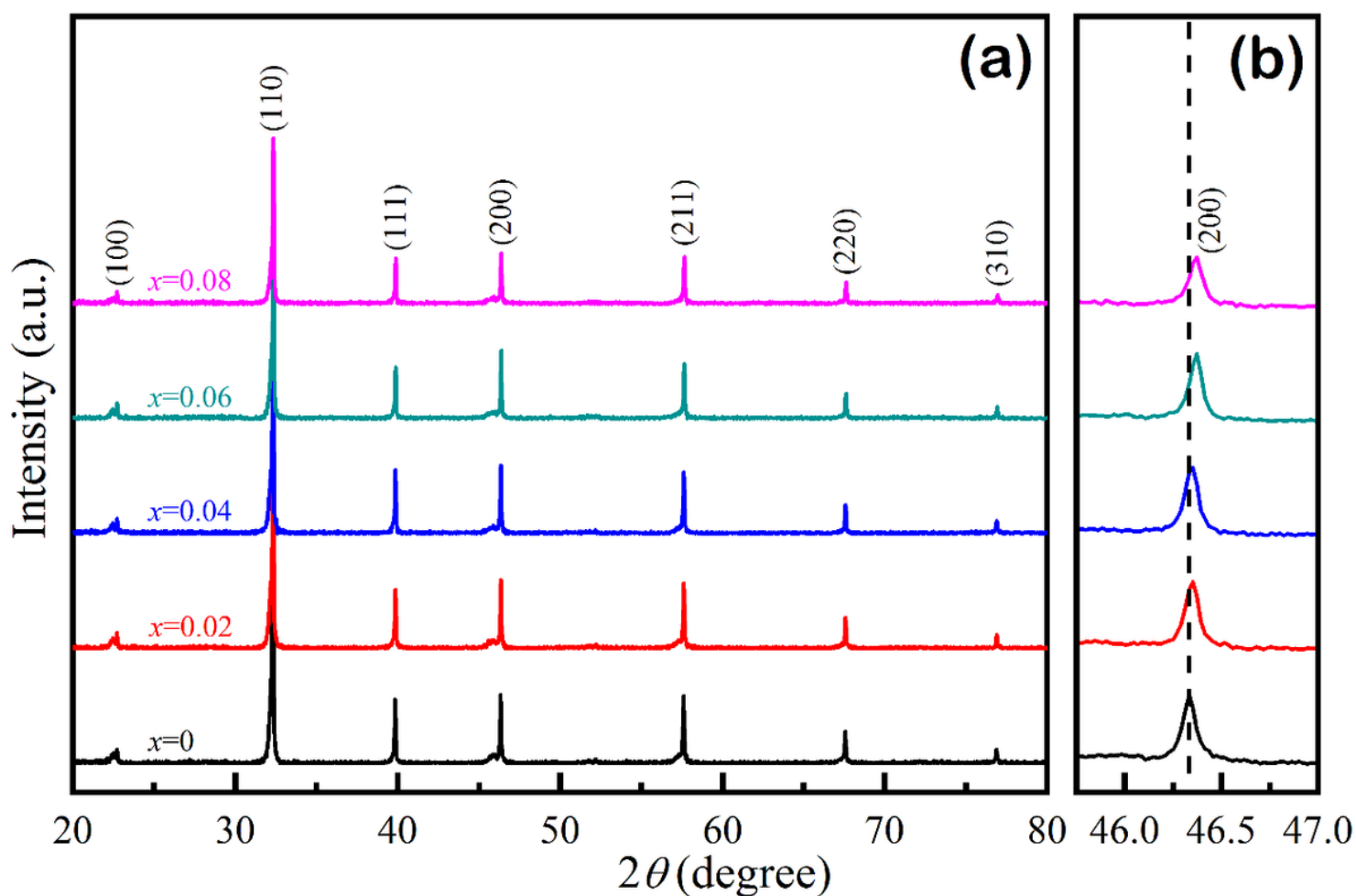
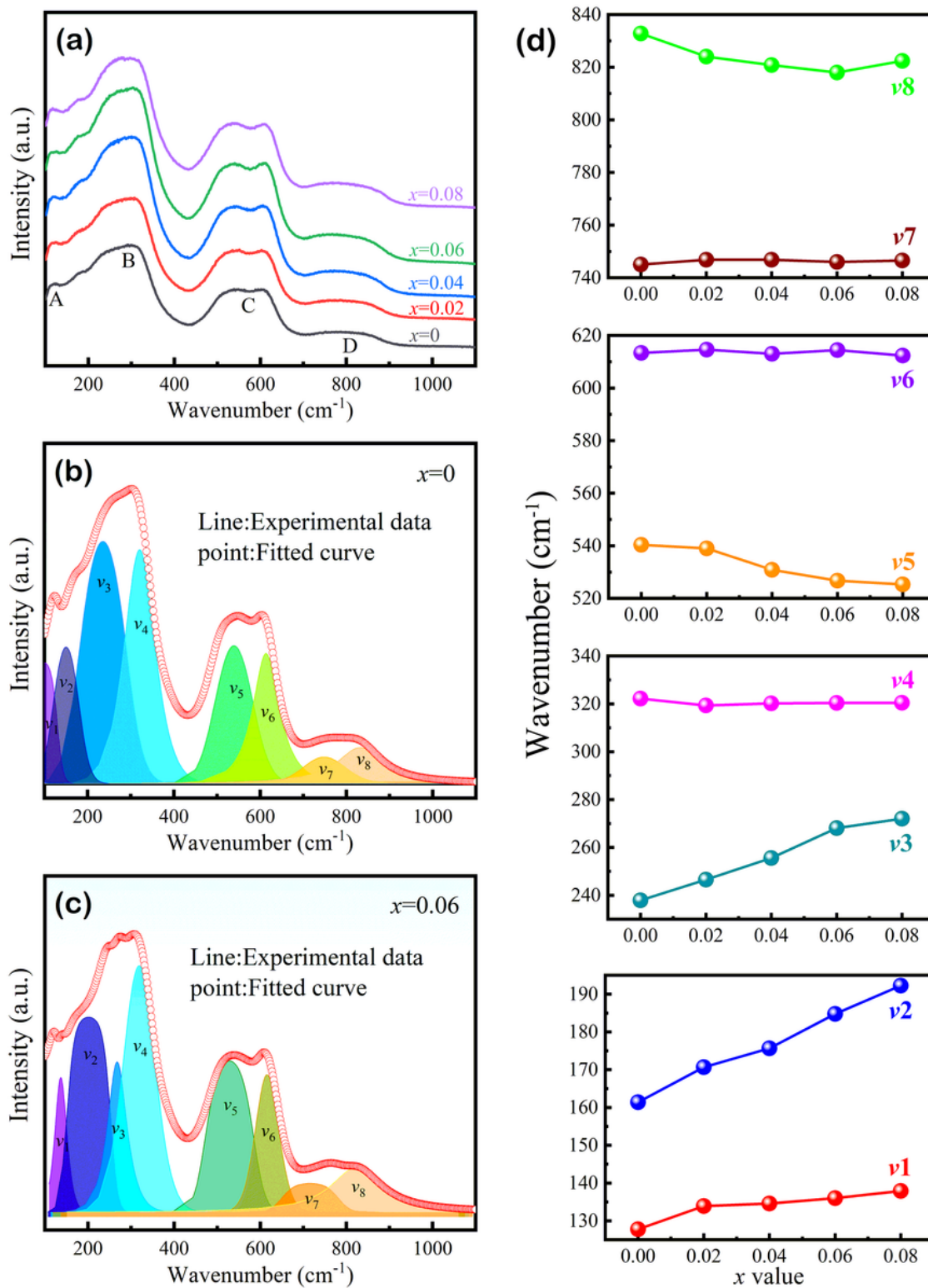


Figure 1

XRD patterns of BNS0.245-1.5x $\delta$ 0.5xB0.325+xT ceramics: (a)  $2\theta = 20^\circ$ - $80^\circ$  and (b)  $2\theta = 46^\circ$ - $47^\circ$ .



**Figure 2**

(a) Raman patterns of BNS0.245-1.5x $\delta$ 0.5xB0.325+xT ceramics at room temperature. Lorentz peak fitting of Raman pattern for represented BNS0.245-1.5x $\delta$ 0.5xB0.325+xT ceramics with (b) x=0 and (c) x=0.06. (d) Wave number of Raman peaks from v1 to v8 of BNS0.245-1.5x $\delta$ 0.5xB0.325+xT ceramics as a function of x value.

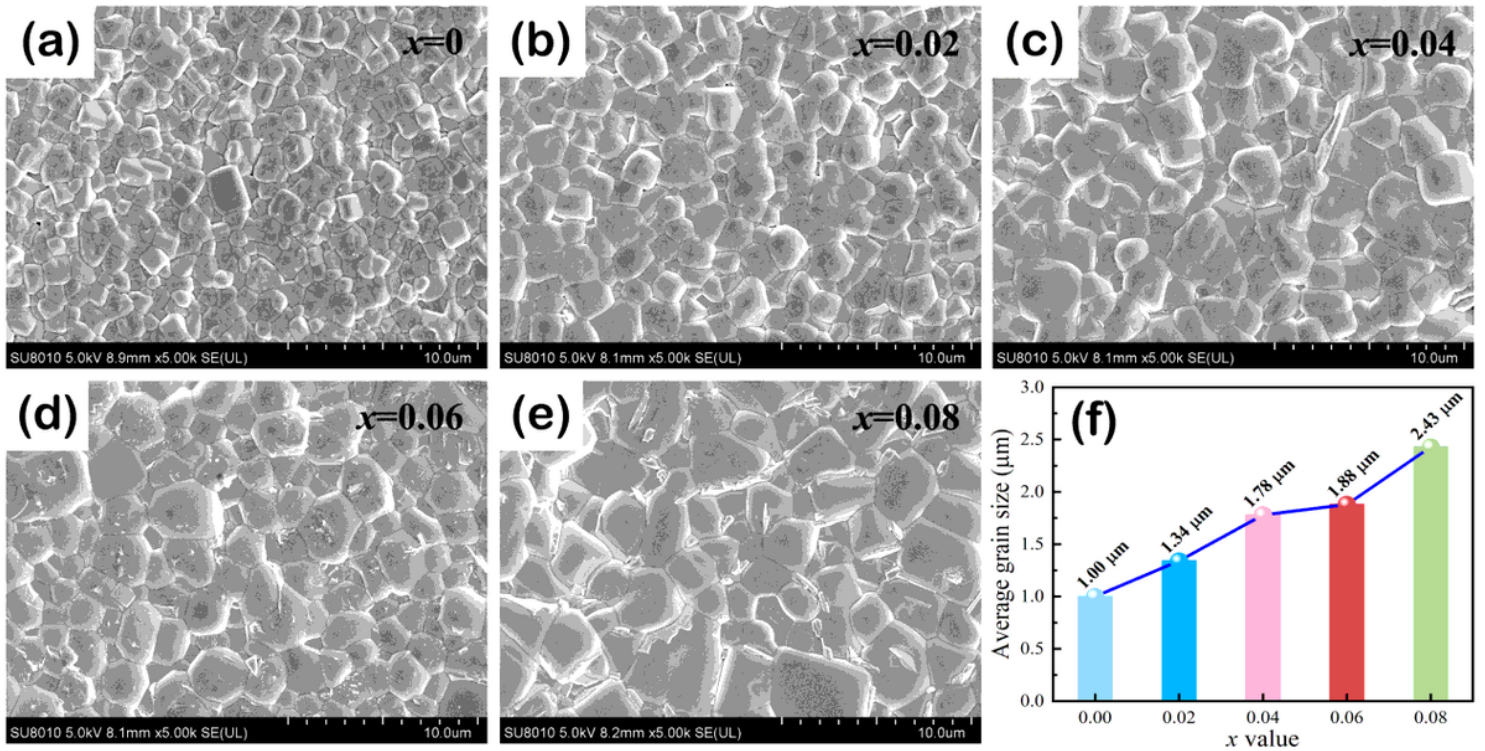


Figure 3

SEM images of polished and thermally-etched surface of BNS0.245-1.5xδ0.5xB0.325+xT ceramics: (a) x=0, (b) x=0.02, (c) x=0.04, (d) x=0.06, and (e) x=0.08. (f) The average grain size of BNS0.245-1.5xδ0.5xB0.325+xT ceramics as a function of x value.

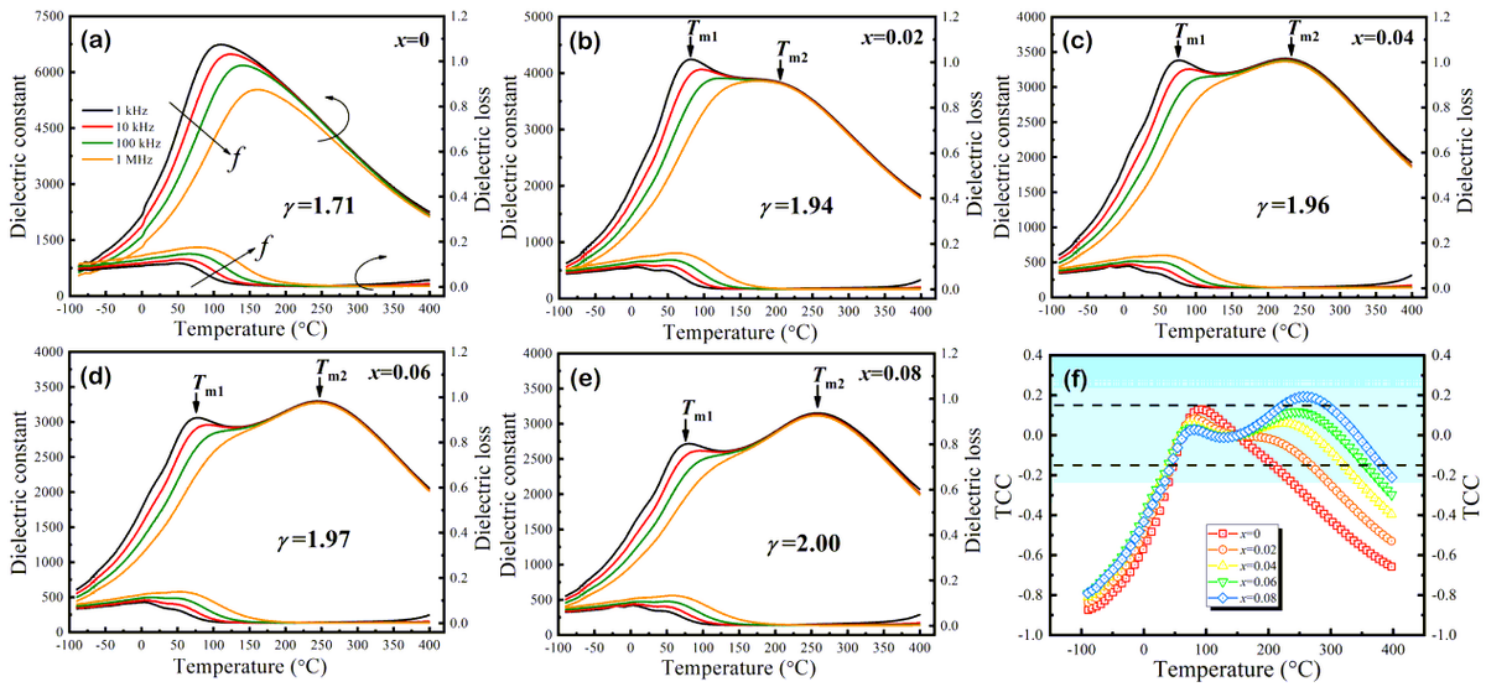


Figure 4

Temperature dependent dielectric constant and loss of BNS0.245-1.5xđ0.5xB0.325+xT ceramics at typical frequencies: (a) x=0, (b) x=0.02, (c) x=0.04, (d) x=0.06, (e) x=0.08. (f) Temperature stability of dielectric constant for BNS0.245-1.5xđ0.5xB0.325+xT ceramics with different x values chosen 150 °C as based temperature.

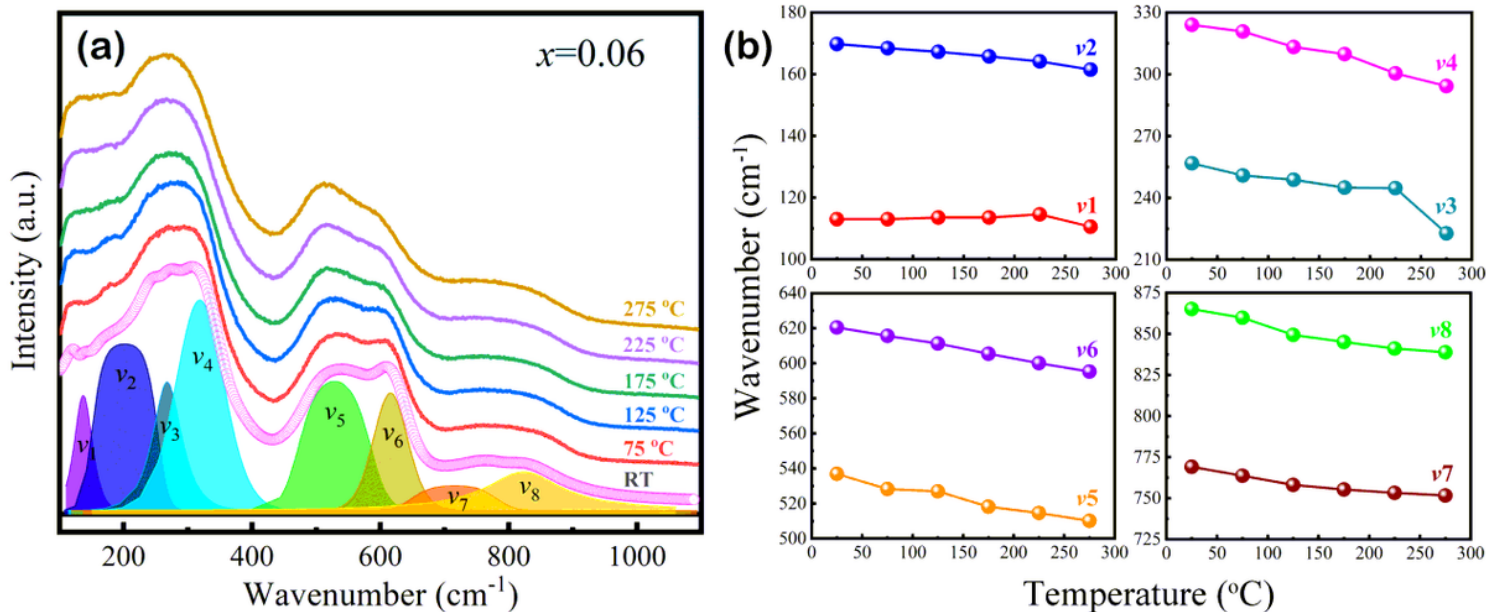
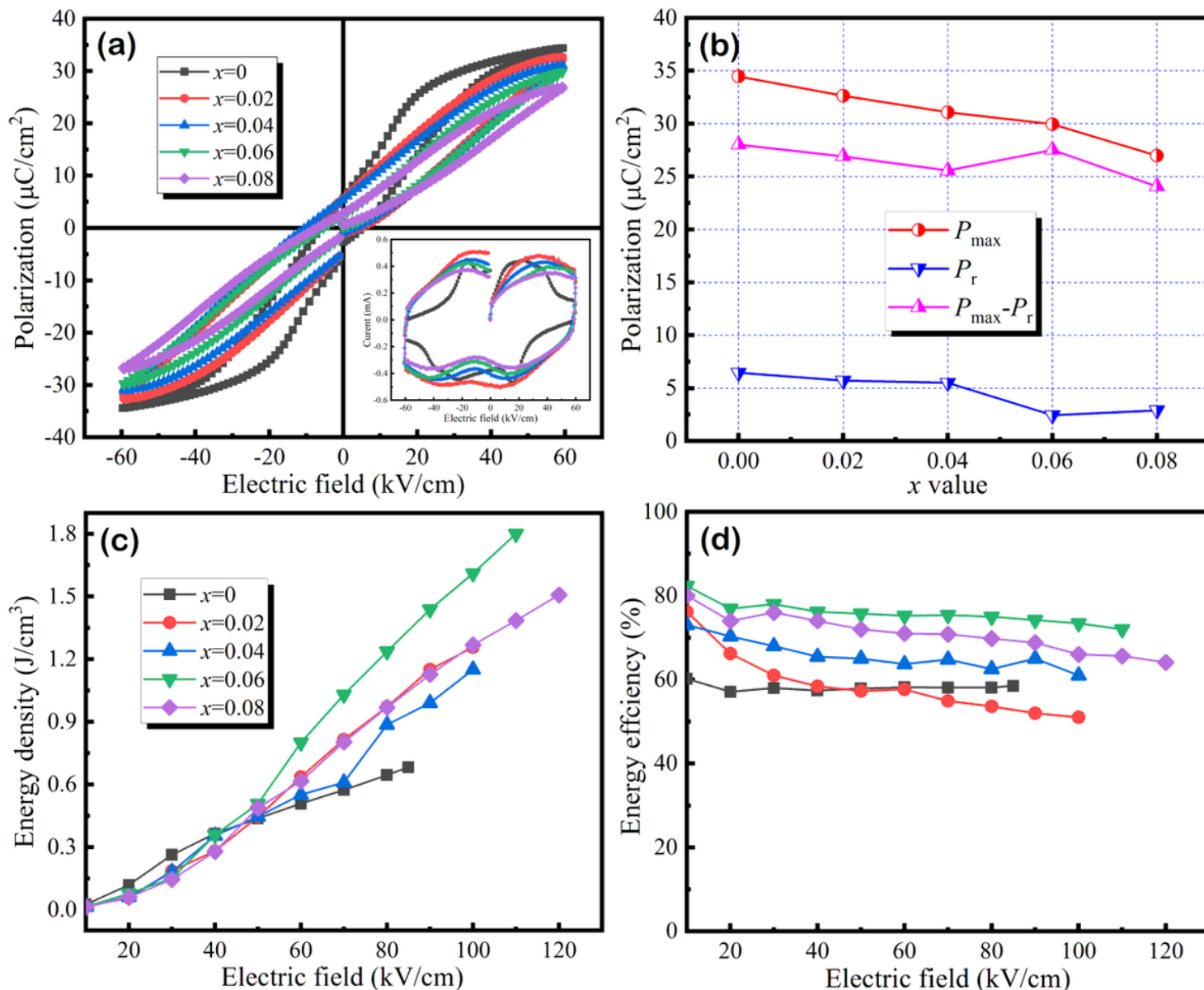


Figure 5

(a) Raman spectra and (b) wave number of Raman peaks from  $\nu_1$  to  $\nu_8$  of BNS0.245-1.5xđ0.5xB0.325+xT ceramics with  $x = 0.06$  at different temperatures.



**Figure 6**

(a) P-E loops measured at 60  $\text{kV}/\text{cm}$  for BNS0.245-1.5xδ0.5xB0.325+xT ceramics with different x values. The insert shows the corresponding I-E loops. (b)  $P_{\text{max}}$ ,  $P_r$  and  $P_{\text{max}} - P_r$  versus x value for BNS0.245-1.5xδ0.5xB0.325+xT ceramics at 60  $\text{kV}/\text{cm}$ . (c) Recoverable energy density  $W_{\text{rec}}$  and (d) energy efficiency  $\eta$  as a function of applied electric field for BNS0.245-1.5xδ0.5xB0.325+xT ceramics.

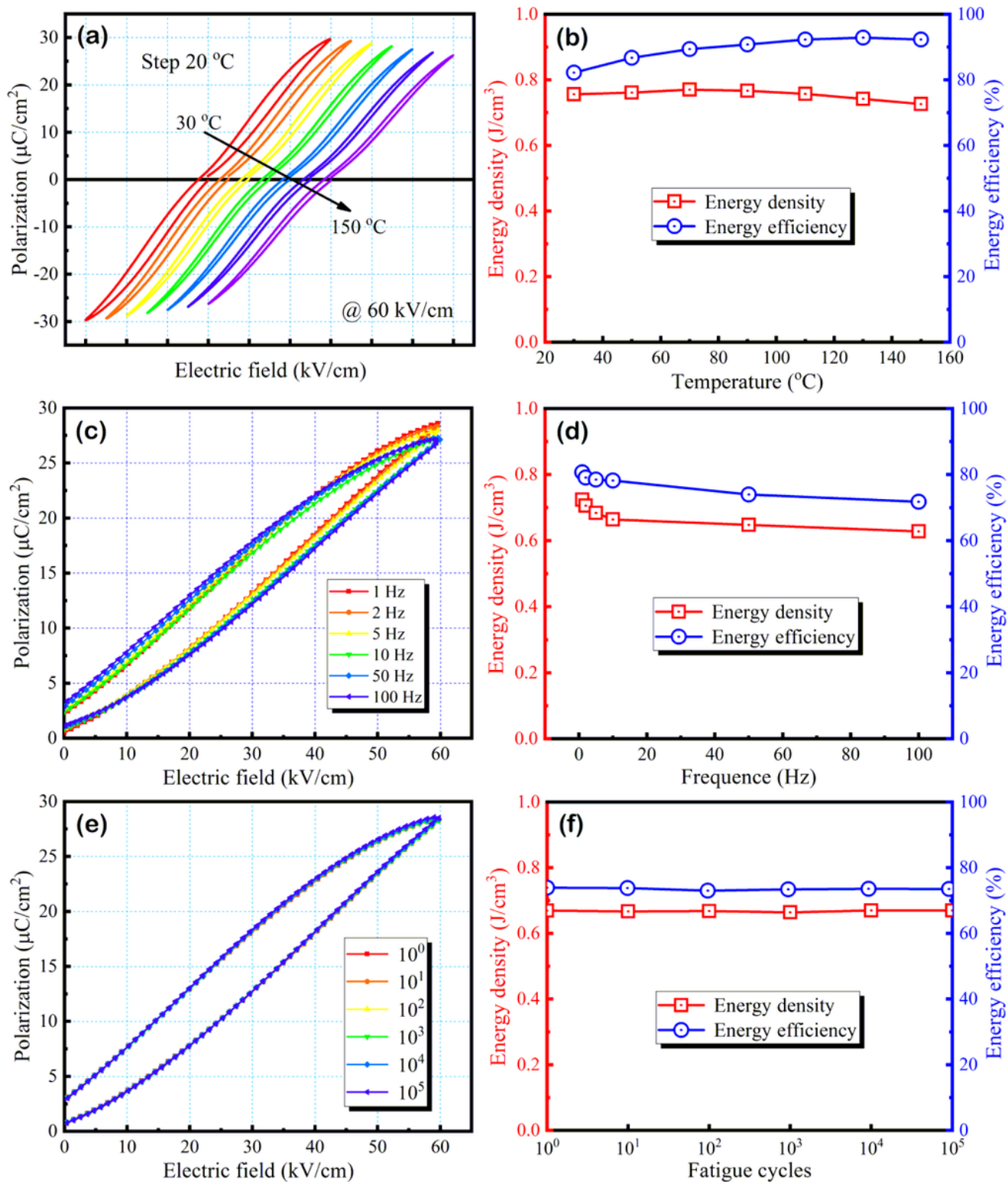


**Figure 7**

P-E loops as a function of (a) temperature, (c) frequency, and (e) cycle numbers for BNS0.245-1.5x0.5x0.325+xT ceramics with x = 0.06.  $W_{\text{rec}}$  and  $\eta$  as a function of (b) temperature, (d) frequency, and (f) cycle numbers for BNS0.245-1.5x0.5x0.325+xT ceramics with x = 0.06.

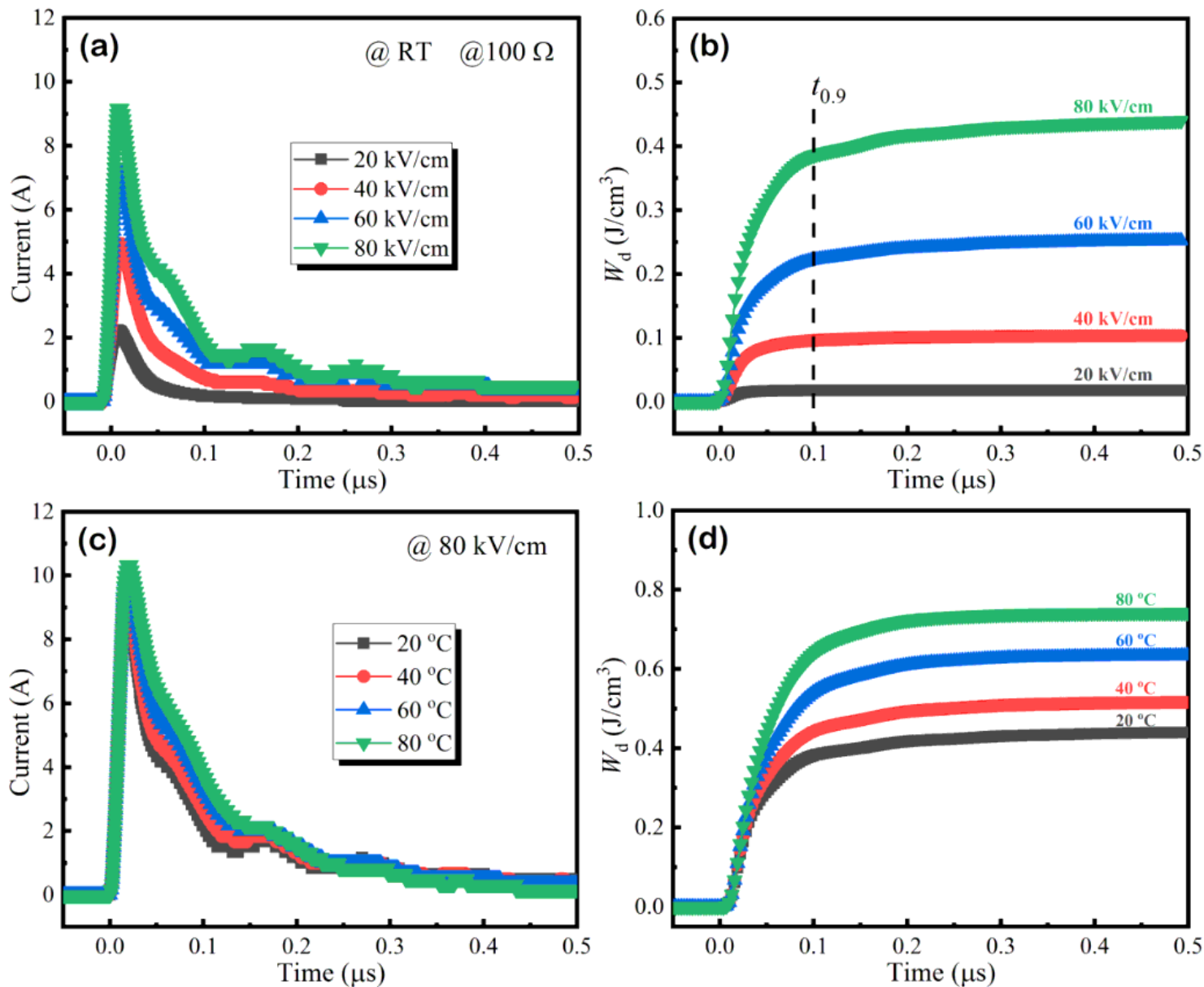


**Figure 8**

(a) Overdamped discharge current curves and (b) corresponding discharge density  $W_d$  as a function of electric field for  $x = 0.06$  ceramics at room temperature. (c) Overdamped discharge current curves and (d) corresponding discharge density  $W_d$  as a function of temperature for  $x = 0.06$  ceramics at 80 kV/cm.

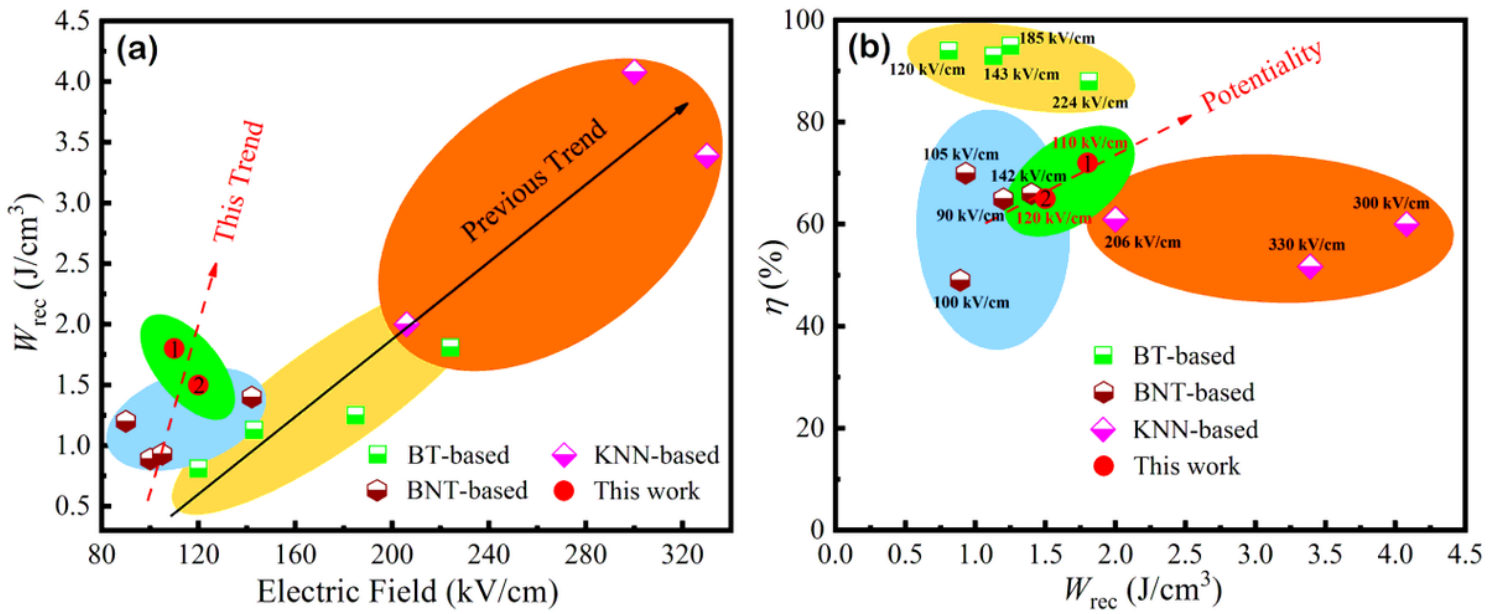


**Figure 9**

A comparison of energy storage properties ( $W_{rec}$  and  $\eta$ ) between some reported lead-free ferroelectric ceramics and this work. Note that 1 and 2 in the red ball denote the  $x = 0.06$  and  $x = 0.08$  compositions in this work, respectively.